LAWRENCE
LIVERMORE
NATIONAL
LABORATORY

UCRL-TR-215180

X-Ray CT of Highly-Attenuating Objects: 9- or 15- MV Spectra?

G. Stone, J. Trebes, R. Perry, D. Schneberk, C. Logan

September 8, 2005

This work was performed under the auspices of the U.S. Department of Energy by University of California, Lawrence Livermore National Laboratory under Contract W-7405-Eng-48.

X-Ray CT of Highly-Attenuating Objects: 9- or 15-MV Spectra?

Gary Stone, Jim Trebes, Roger Perry, Dan Schneberk and Clint Logan
Lawrence Livermore National Laboratory
August 28, 2005

Executive Summary

We imaged-highly attenuating test objects in three dimensions with 9-MV[1] (at LLNL) and 15-MV (at Hill Air Force Base) x-ray spectra. While we used the same detector and motion control, there were differences that we could not control in the two radiography bays and in the sources. The results show better spatial resolution for the 9-MV spectrum and better contrast for the 15-MV spectrum. The 15-MV data contains a noise pattern that obfuscates the data.

It is our judgment that if sufficient attention were given to design of the bay, beam dump, collimation, filtration and linac spot size; a 15-MV imaging system using a flat panel could be developed with spatial resolution of 5 lp/mm and contrastive performance better than we have demonstrated using a 9-MV spectrum.

Introduction

Assemblies consisting of substantial thicknesses of high-density, high-Z material present challenges for high-resolution (5 lp/mm or higher) 3D x-ray CT inspections. The most penetrating x-ray energies for these materials are near 3.5 MeV[1]. Spectra containing these x-rays produce large amounts of Compton scatter from the object, from the collimators, from the detector, from the beam dump and the surroundings. Some of this scatter interacts with the detector and imposes limitations on the spatial resolution and contrastive performance of digital radiography (DR) and computed tomography (CT) inspections. At the same time, objects of this type are often of high value with high consequence of failure creating a need for quality nondestructive inspection information however obtained.

[1] We use voltage (MV) to describe sources or spectra, energy (MeV) to describe electron or x-ray energy and hyphens when they are adjectives.

Commercial electron linacs are available that accelerate electrons to energies up to 24 MeV. These electrons are stopped in a (usually) tungsten target producing a bremsstahlung spectrum with endpoint energy equal to the incident electron energy. Spectra from 9-and 15- MV linacs are presented in Figure 1. These spectra have been normalized so that the integral over energy is one x-ray. Accelerating potentials below 9 MV are not very useful for objects of interest here because insufficient x-rays are produced near 3.5 MeV. LLNL operates a 9-MV linac. The question often arises whether the spectrum produced by higher electron energies might improve image fidelity. Certainly higher electron energy will produce more of the desired x-rays for either fixed electron current or electron beam power. Higher electron energy will also produce x-rays above 7 MeV that have little likelihood of contributing to an image in assemblies considered here (discussed in more detail later). These x-rays *may* also give rise to another set of imaging challenges because of the onset of significant pair production.

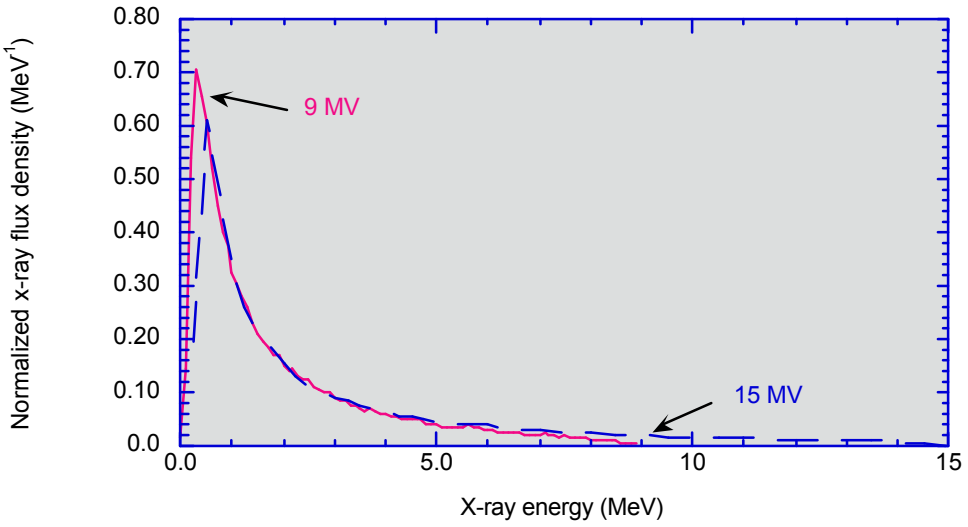

Figure 1 **Calculated spectra for 9-MV and 15-MV electron linacs. These have been normalized so that the energy integral is unity.** ***[Schach von Wittenau, 2002a, 2005]***

We report here the results of imaging tests comparing images from the LLNL 9-MV source with images from the Hill Air Force Base (AFB) 15-MV source.

THE LLNL SYSTEM AND MV IMAGING BASICS

At LLNL we are developing CT systems, methods and analysis tools for high-spatial-resolution, high-energy DR/CT inspections of components and assemblies. Integral to this effort are detailed Monte Carlo modeling studies and supporting scans of test objects *[Aufderheide, 2000; Aufderheide, 2002; Logan, 2001; Schach von Wittenau, 2001; Schach von Wittenau, 2002a; Schach von Wittenau, 2002b; Schach von Wittenau, 2002c; Waters, 1999a and Waters, 1999b]*. One currently-fielded system utilizes an optimized collimator for area detectors, a Thales amorphous silicon (Am-Si) FlashScan 33 detector, Newport air bearing table and motion control hardware, and a 9-MV Varian Linatron

3000 that has been modified to reduce the spot size to a measured 1.1-mm FWHM *[Schach von Wittenau, 2002a]*. Figure 2 shows the linac, collimator, staging and detector. We used important elements of this detector system to scan the same set of assemblies at LLNL (9 MV) and at Hill AFB (15 MV).

In general, the components of detector response in high-energy (MeV) contexts are the same as other x-ray imaging acquisition. Given a detector element in space at position ζ_D, and size ν, on a line from the x-ray source with energy E (possibly a spectrum), at position ζ_S, through the object centered at ζ_O: the total photons, $N_T(\zeta_D, \nu, E)$, divide into two types, $N_P(\zeta_D, \nu, E)$, and $N_S(\zeta_D, \nu, E)$, primary and scatter respectively. Scattered photons arise from the object, $N_{SO}(\zeta_D, \nu, E)$, the experimental fixtures (collimators, room, walls, etc), $N_{SBK}(\zeta_D, \nu, E)$, and scatter from within the detector itself $N_{SD}(\zeta_D, \nu, E)$ *[Schach von Wittenau, 2002a]*.

$$N_T(\zeta_D, \nu, E) = N_P(\zeta_D, \nu, E) + N_S(\zeta_D, \nu, E),$$

$$N_S(\zeta_D, \nu, E) = N_{SO}(\zeta_D, \nu, E) + N_{SBK}(\zeta_D, \nu, E) + N_{SD}(\zeta_D, \nu, E)$$

Also, the photons from the source to detector without the object in the field of view, $N_{To}(\zeta_D, \nu, E)$, is approximately given by:

$$N_{To}(\zeta_D, \nu, E) \cong N_{Po}(\zeta_D, \nu, E) + N_{SBK}(\zeta_D, \nu, E) + N_{SD}(\zeta_D, \nu, E)$$

Independent of the type of detector, MeV x-ray imaging is distinctive in the proportions of the different types of photons. First, the proportion of scattered photons is higher. Compton scatter is the dominant attenuation mechanism in the MeV range. Also, few primary[2] photons penetrate the object to produce an image. Consequently, $N_{SO}(\zeta_D, \nu, E)$ is absolutely and proportionately higher, especially for hard-to-penetrate high-Z components and assemblies. Further, the values of $N_{SBK}(\zeta_D, \nu, E)$ and $N_{SD}(\zeta_D, \nu, E)$ can be higher depending upon the room, the collimator, the surrounding objects, and the physical construction of the detector. While scatter from the object is a ubiquitous part of the inspection, the best imaging is performed when the values "Background" scatter and "Detector" scatter are as small as possible. Photon counts from these sources convey little information about the object, add statistical noise and consume valuable dynamic range in the detector. Scintillator-based detectors have higher response to scatter photons (because they are lower in energy) than to primary photons. Detector scatter in particular acts like a blurring function, degrading spatial performance. Further, CT reconstruction algorithms do not consider scatter, but proceed as if all detector response arises from photons traversing straight lines from the source through the object to the detector. Scatter generates artifacts in the reconstructed images.

[2] We use primary to designate photons coming from the source without an intervening scatter event.

At LLNL, 13 years of analysis and experimentation has led us to the following principles for high-energy CT imaging:

1. **Compared to all other configurations used or analyzed, we observe an advantage for Stonehenge II collimator panels at 1 meter, 3 meters and 5 meters from the x-ray source with graded, tapered, thick, high-Z apertures matching the beam divergence. It is better to arrange collimation so that the "beam" is slightly larger than the area used for active imaging. If the full area of the fixed Stonehenge II collimation is not required it is best to further collimate at the 3.1-meter collimator position, and use the 5-meter position to clean up some of the scattered photons made by the additional collimation in the beam at 3.1 meters *[Schach von Wittenau, 2001]*.**
2. **For the "Stonehenge II + Middle collimator" arrangement, the "tail" of collimator scatter extends inward roughly 38 mm from the geometric edge of the beam. It is best when the object does not fall within the 38-mm "tail" border. However, there are benefits for area detectors to collimate to just greater than the area of the object plus the 38 mm on all sides of the object.**
3. **For area detectors with thin screens (in particular Am-Si detectors with Lanex Fine screens), filtering the 9-MV source with modest thickness of high-Z materials near the source improves contrast for highly attenuating chord lengths. We employ 4 to 12 mm of tantalum at the LLNL 9-MV linac for imaging high-Z components and assemblies.**
4. **It is best to use high-Z materials for any location exposed to direct source photons. This is because fewer x-rays are reflected back into the room space. *[Logan, 2001]***
5. **It is important to avoid placing materials (scattering mass) within 10 feet behind the detector. Using a 2-inch-diameter, 6-inch-long tungsten cylinder, we measured increased counts in the shadow of the cylinder from a 2 ft. slab of concrete placed 10 feet behind the detector. While 10 feet was the distance at which detected counts fell at or below the overall counts from other scatter sources, we normally configure a 50-ft beam dump for 9-MV imaging. *[Logan, 2001]***
6. **The best high-energy area imaging detectors are thin. Structural material behind the active detector in the Flashscan 33 panel is a large source of detector scatter. *[Schach von Wittenau, 2000]***

(a)

(b)

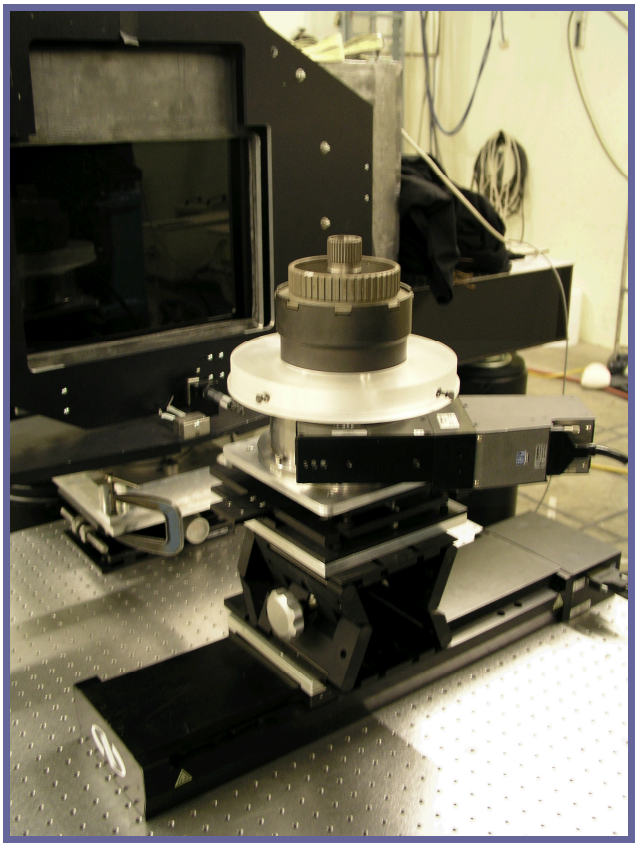

(c)

Figure 2 **LLNL Linac source on right in (b) along with the Stonehenge II collimator in (a) & (b). Image (c) shows the object positioning system and Thales 14-bit Am-Si imaging panel. These components were used for image acquisition at both LLNL and Hill AFB.**

TEST OBJECTS

To experimentally compare the performance of 9- and 15-MV bremsstahlung spectra we configured a modular assembly of light materials encased by heavy materials. We built our assemblies from concentric cylinders of polyethylene, lead, aluminum, tungsten and steel. The greatest challenge for contrastive performance at these energies is the detection of small features in low-Z, low-density components encased in substantial amounts of high-Z, dense material. The W object is property of Atomic Weapons Establishment at Aldermaston, Great Britain (AWE) who graciously permitted its use for this work.

Figure 3 is a drawing of the full test object assembly, identifying the materials and the thickness for the different components. The innermost cylinder is polyethylene ($Z<6$, density 1.425 g/cm^3), 50.8-mm diameter, cut through the axis into two halves with different sized holes drilled in the inner face of one half, and in the outer face of the second half. Figure 4 contains a photo of the two halves of the polyethylene cylinder. Figure 5 shows the details on the diameters of the center holes and the outside holes of the polyethylene half-cylinders. The assembled polyethylene cylinder is inserted into a 101.6-mm diameter, 25.4-mm wall thickness lead pipe. The poly-lead assembly is then inserted into a 127-mm diameter, 12.7 mm wall thickness aluminum pipe. This is the base object assembly. Additional rings of W and stainless steel are added to increase imaging difficulty. Scans will be compared on the basis of detection and contrast of small features in the polyethylene and in the W ring when present.

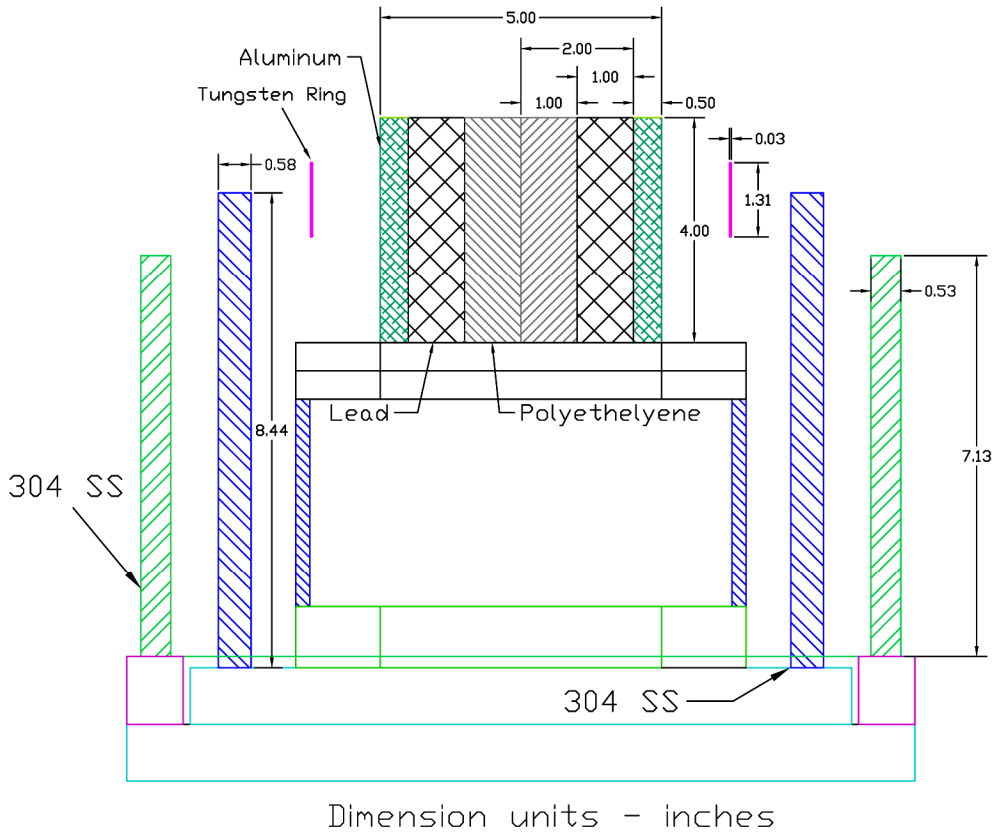

Figure 3 **Drawing of full assembly of cylindrical objects, polyethylene, lead, aluminum, tungsten, and two 304 stainless steel outer rings.**

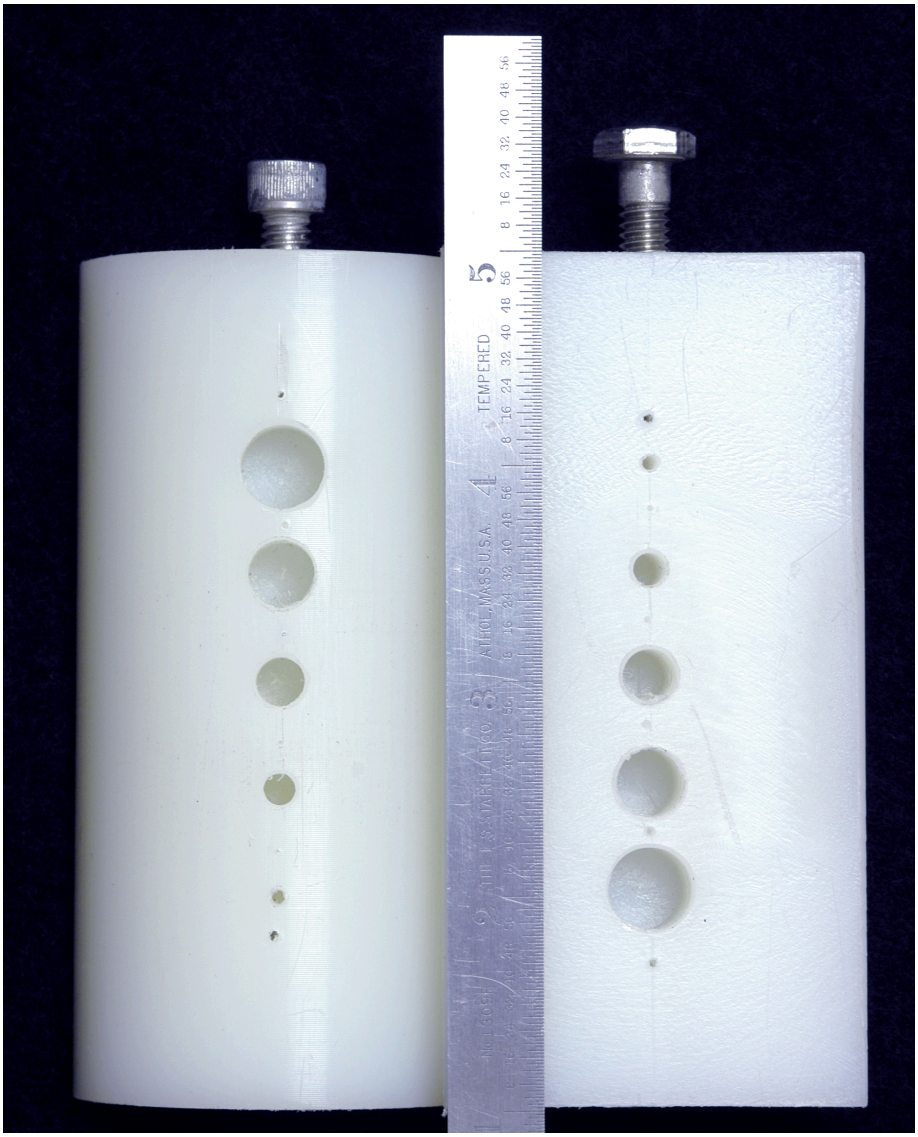

Figure 4 **Photograph of polyethylene half-cylinder inserts with holes in the center interface and on the outside surface of the composed cylinder**

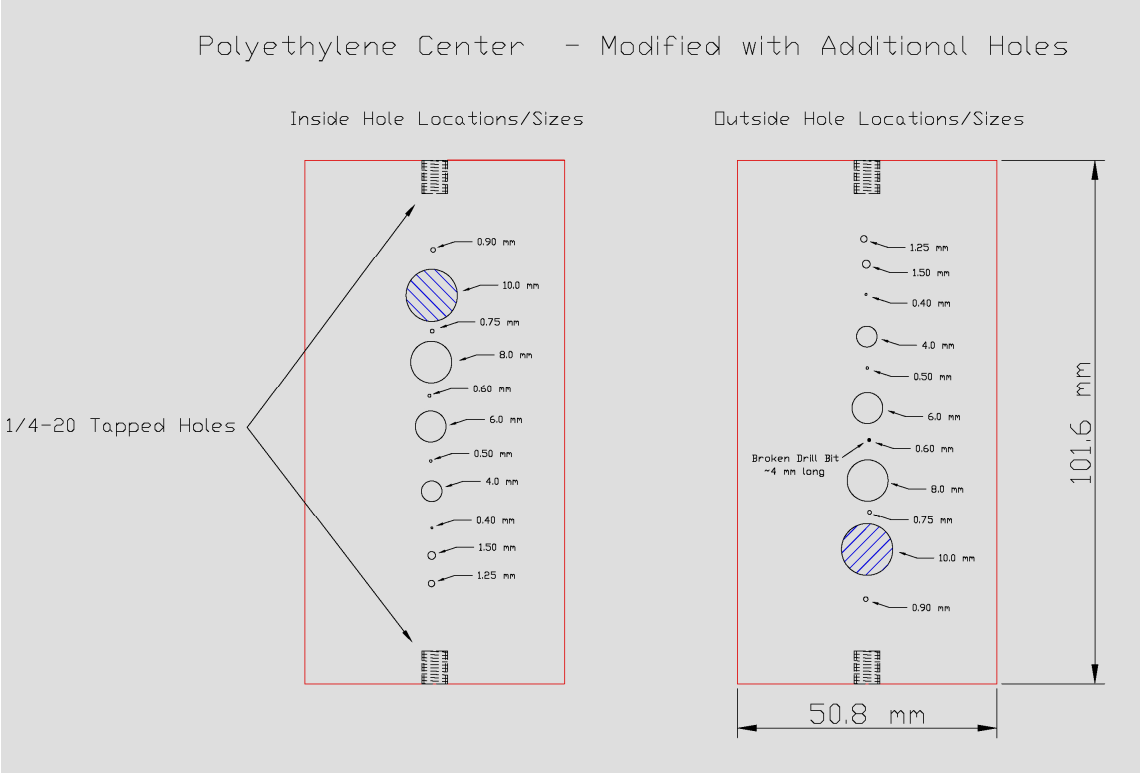

Figure 5 **Drawing of polyethylene half-cylinder inserts with holes dimensions and locations. Hole depths are not controlled.**

High-Z assemblies often include detailed features in the high-Z material. AWE has fabricated a tungsten ring with small voids on the inner surface. The ring is 194.5 mm in diameter with a 1.9-mm wall thickness and is 30.2-mm high. The features on the inside surface of the ring vary in size and depth from 1.9-mm diameter by 0.4-mm depth to 0.137-mm diameter and 0.052-mm depth (see Figure 6).

The last two components of the assembly are two approximately ½-inch-thick 304 stainless steel rings of different heights, one with a 10.75 inch outer diameter, and one with a 13.5 inch outer diameter. These two components do not contain features, but are included to add attenuation and scatter to the imaging of features in the polyethylene and tungsten. Figure 7 presents digital photos of two different assemblies mounted on the positioning system fielded at Hill AFB for 15-MV scanning. The same configurations were subsequently scanned at LLNL using the 9-MV spectrum.

Figure 8 presents a plot of the calculated transmission as a function of energy for the long and short chords through the Al-Pb-polyethylene test assembly for energies from 500 keV to 10 MeV. We define the long chord to be tangent to the inside diameter of the Pb cylinder. The short chord passes through the Pb cylinder on axis. Notice the decrease in transmission as energy increases beyond 5 MeV. For the long chord, x-ray transmission peaks between 3 and 4 MeV at a value of approximately 1.2% while the short chord transmission is about 5.9% at approximately the same energy. Traditionally,

computed tomography is best performed at 13% transmission *[Grodzins, 1983]*. The relatively low level of transmission here means even small sources of scattered signal can effectively "hide" subtle features in the low-Z material. So, for this imaging task, x-rays between 2 and 7 MeV are the important photons for image formation and even at these energies, we are far below optimum transmission. Photons outside this energy range are not transmitted sufficiently to be strong contributors to the desired image.

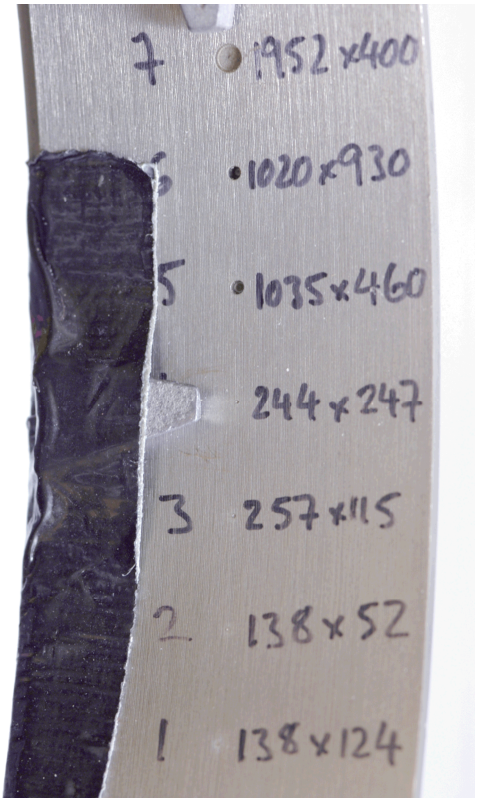

Figure 6 **Photograph of inside surface of AWE tungsten ring showing holes and dimensions (diameter & depth in µm. Dark area is tape securing a Pb fiducial.**

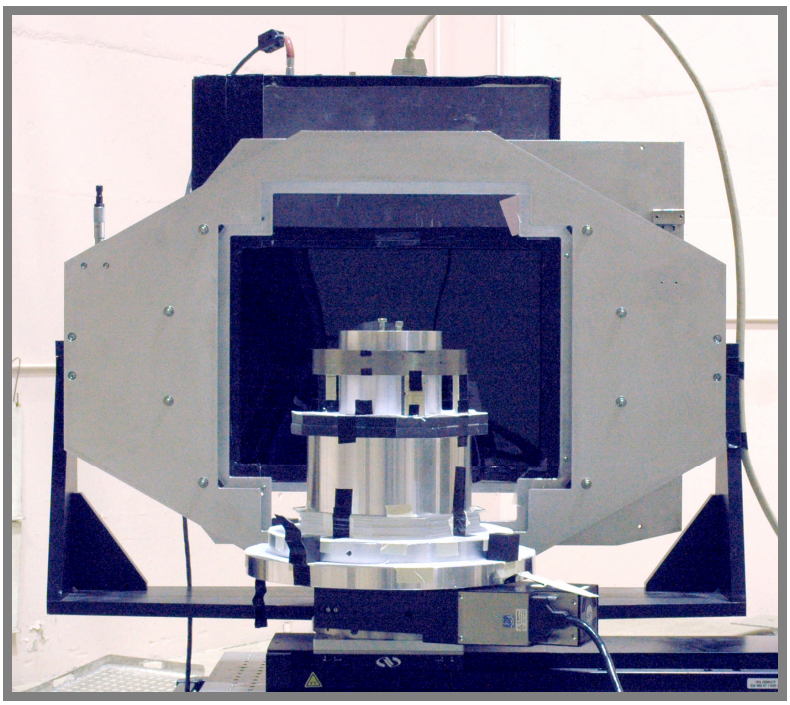

(a)

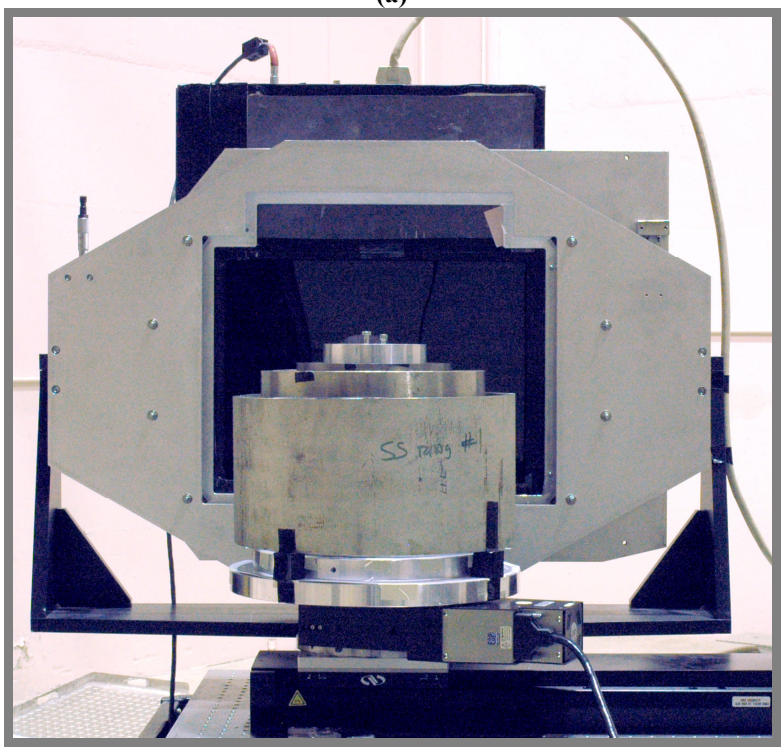

(b)

Figure 7 (a) Al-Pb-polyethylene assy. + W ring at Hill AFB. (b) Thickest test object with two stainless steel rings

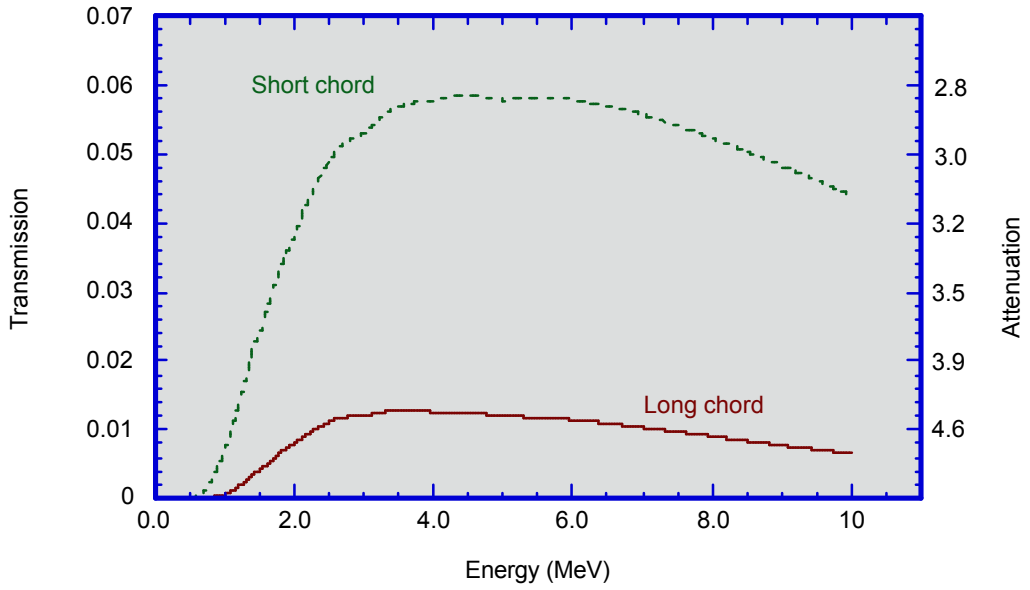

Figure 8 **Computed transmission as a function of x-ray energy for two chords through the Al-Pb-polyethylene test object. Right axis shows corresponding values of attenuation [-ln (transmission)].**

Scan Parameters

We made the 9-MV scans and the 15-MV scans as nearly identical as possible. Both sets of scans were acquired with a Thales Flashscan 33 Am-Si panel, manipulator and portable scanning table, transported to the two different locations. Test object assemblies were exactly the same. Each data set contained 900 views acquired over 360 degrees. Distances from source to detector, object to detector were roughly the same, with some adjustment made to minimize the impact of the larger spot size at HILL AFB. We were not able to transport, deploy and align the Stonehenge II collimator to the Hill AFB x-ray source. Instead we configured two tungsten collimators, installed on portable tables, and aligned them to the source-detector beamline at Hill.

Figure 9 is a drawing of collimator, detector and object placement fielded at Hill AFB. The primary (closest to linac) collimator was a set of W blocks supported on an Al frame. That assembly was mounted on the centerline of an existing tungsten collimator used at LLNL. The total thickness of tungsten in the primary collimator was 7.75 inches. The secondary collimator at Hill AFB was adapted from a source collimator salvaged from a 9-MV linac head. The total thickness of tungsten in the secondary collimator was 5.475 inches. The unattenuated aperture for these collimators was set in a horizontal image format 14.5 inch x 5.5 inches at the detector. This size and aspect ratio was chosen to match the test objects selected for this series.

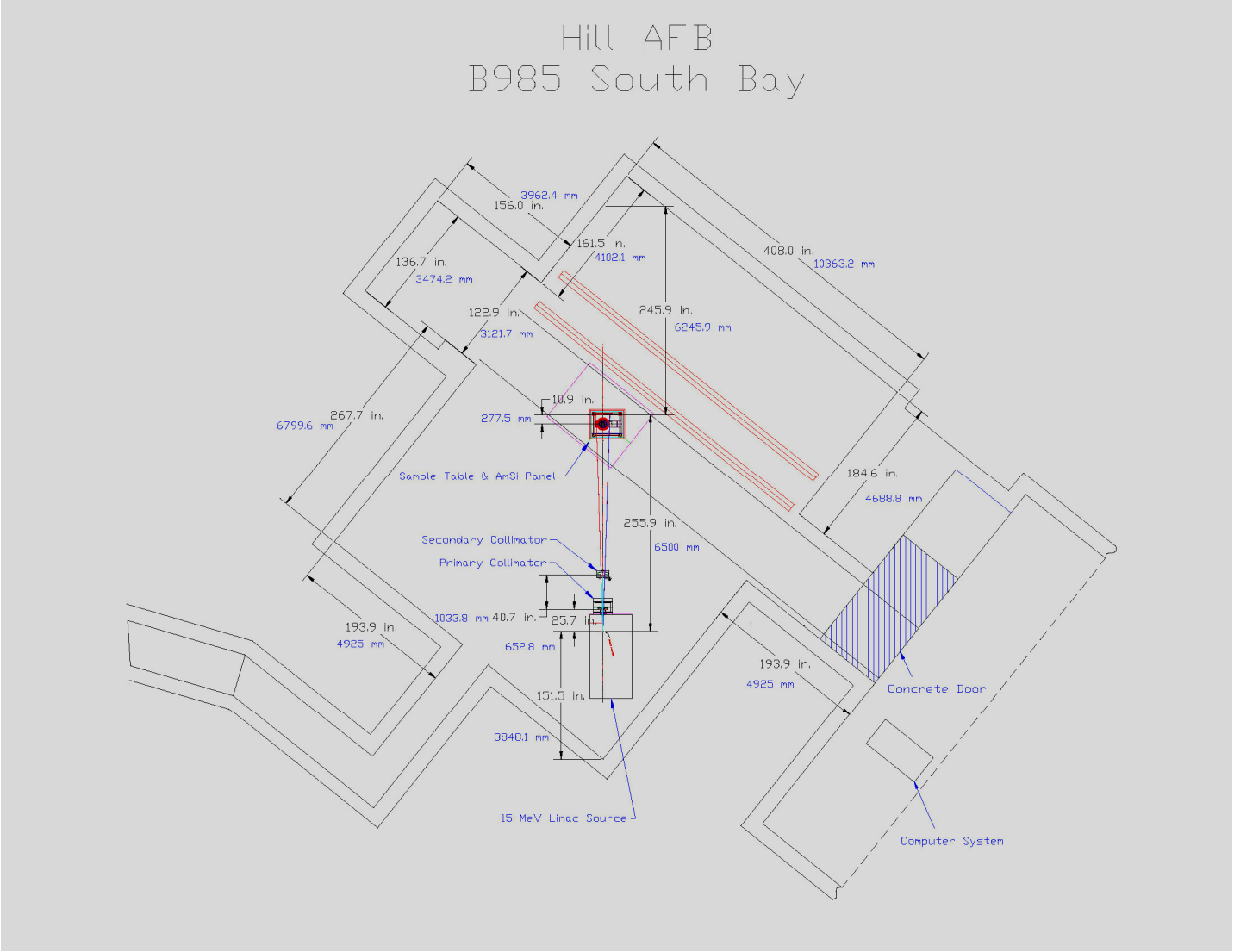

Figure 9 Drawing of Scanner components as fielded in the 15-MV bay at Hill AFB

Table 1 Scan parameters for two high-energy spectra

	9-MV spectrum	15-MV spectrum
Facility	LLNL nine bay B239	Hill AFB B985 S. Bay
Imager & motion control	LLNL system	LLNL system
Test Objects	same	same
# views & angular range	900 views; 360 °	900 views; 360 °
Integration time & replicates	1.8 s & 6 frames	1.8 s & 6 frames
Collimator	Stonehenge II + supplemental	2 stage W ; 13 inches tot.
Source-to-detector	5,751 mm	6500 mm
Object-to-detector	355 mm	277 mm
Spot size	1.1 mm	2.2 mm
Source penumbral blur	68 μm	94 μm
Filtering	6.3 mm Ta	38-mm stainless steel [§]

[§] The Hill linac is fitted with a "field flattener" for the purpose of making the x-ray beam more uniform over the solid angle used for film imaging. The unmodified beam has more photons on the beam axis than away from the axis. This is generally not desired for work with film because of its limited dynamic range. The flattener is an axisymmetric blob shape that is thickest on the beam axis. Thickness listed is on axis.

The arrangement we chose at Hill AFB placed the test object and detector in the middle of the room to minimize the amount of backscattered x-rays from the back wall and to approximate the 50-foot beam dump at LLNL. Operational constraints at HILL did not permit the removal of the stainless steel field flattener.

The primary collimator was placed nearly in contact with the source head. The secondary collimator was placed ~60 inches away. Both collimator positions were adjusted using x-ray film to allow alignment without placing the Thales panel in jeopardy from the 15-MV primary x-ray beam. Using 9-MV experience as a guide, we expected substantial scatter from the collimators. To minimize exposure of the Thales panel to this scatter, we placed collimators closer to the source than to the detector. Further, as we had no experience[3] with photodiode panels with a 15-MV source, we used film at the detector position to align the primary and secondary collimators. The Thales detector panel was not deployed until the collimation was confirmed with film to not permit primary beam exposure to the detector electronics. The initial data on the panels also confirmed that we were not damaging the amplifier electronics or detector components of the panels and we were safe to proceed with the CT data collection.

[3] Indeed, to the best of our knowledge there was ***no*** experience with photodiode panels at 15 MV prior to this work.

RESULTS

We present results for three test assemblies:

1) Al-Pb-polyethylene,
2) Al-Pb-polyethylene + W Ring,
3) Al-Pb-polyethylene + W Ring + 2 Stainless Steel rings,

We present comparative ability to resolve small features within the polyethylene and the W ring. We also present signal-to-noise within the uniform polyethylene volume for the different assemblies. Radiographs we present are values of attenuation, where attenuation is defined as $= -\ln(transmission)$.

CT data were preprocessed and reconstructed in exactly the same manner for the various data sets. Slice planes perpendicular to the axis of the assembly are called "horizontal" and slice planes parallel to the assembly axis are called "vertical". The resulting CT data sets are in units of mm^{-1}.

We use the term "lineout" to mean a graphical representation of pixel or voxel data along a line chosen from an image or reconstructed data set.

Al-Pb-polyethylene

Figure 10 presents attenuation radiographs through the assembly for 9-MV and 15-MV spectra. Figure 11 is lineouts through the two attenuation radiographs taken from roughly the same position in the object. Notice the higher attenuation for the 15-MV results. From Figure 8, if scatter were eliminated, the most penetrating of x-rays should have an attenuation of 4.4 on the long chord. Averaged over either spectrum the attenuation should be even higher. The low values of attenuation in Figure 11 indicates that most of the detector response at the longest chord length through the assembly arises from scatter. This is consistent with medical imaging at these energies. *[Siewerdsen, 2001]*. The data also indicate slightly higher contrast for the 15-MV data.

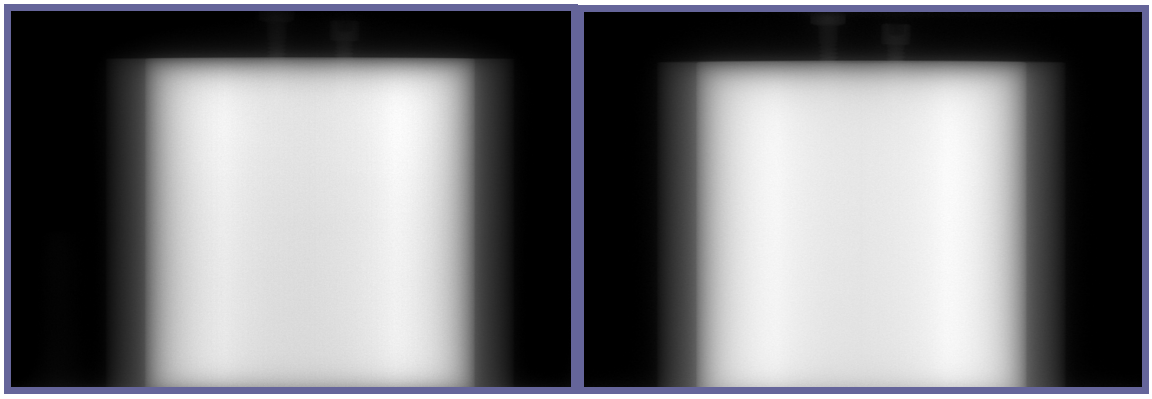

Figure 10 9-MV & 15-MV attenuation radiographs

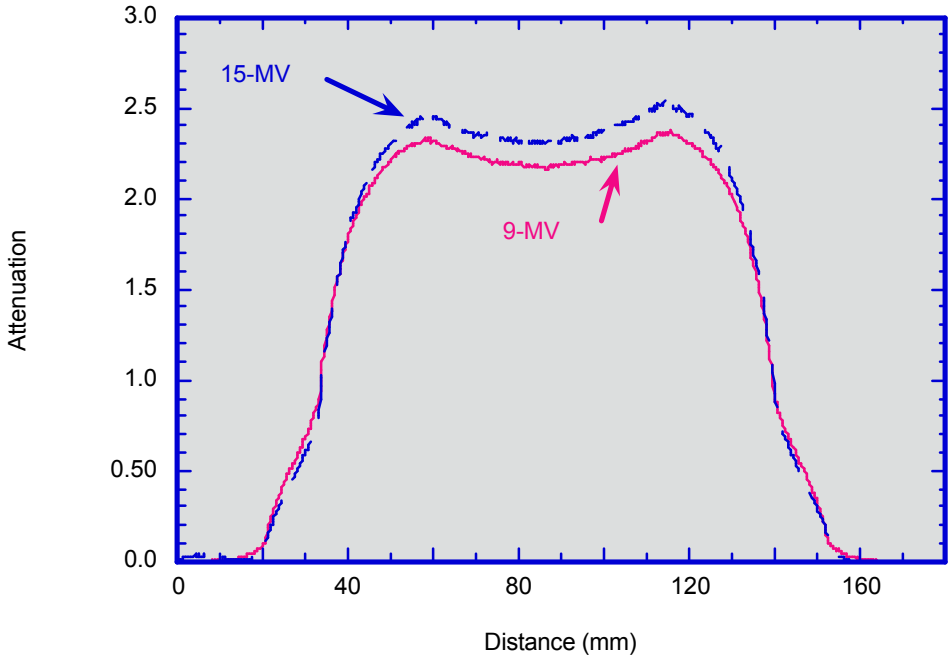

Figure 11 Comparison of attenuation lineouts for 9-MV and 15-MV spectra.

CT data follows the radiographic data. Figure 12 includes two horizontal slices through the Al-Pb-polyethylene phantom. Notice the greater pattern noise in the 15-MV data. As for the holes in the polyethylene, Figure 13 contains averaged vertical slices of the outside polyethylene holes from the two data sets. The largest difference between the 9- and 15-MV lineouts occurs for the smallest feature in the center of the Al-Pb-polyethylene assembly. Figure 15 contains two averaged vertical slices for the center holes in the polyethylene. Notice the sub-millimeter holes are visible in both data sets. Figures 14 and 16 contain lineouts from the different vertical slices showing slightly higher spatial resolution in the 9-MV data and slightly higher modulation contrast in the 15-MV data. We derived signal-to-noise (SNR), the ratio of mean to standard deviation for the same volumes in the separate data sets. The 9-MV data is more strongly affected by cupping artifact (beam hardening), which can lower the measured signal to noise. We attempted to select portions of the volume that minimize this effect. SNRs are presented in Table 2.

Table 2 SNR of two regions for Al-Pb-polyethylene test object.

	9-MV	**15-MV**
Inside holes	36.7	31.4
Outside holes	65.0	52.2

We extracted the images of Figure 17 from reconstructions of horizontal planes in the 9- and 15-MV scans. Notice the noise pattern in the 15-MV data. Figure 17 also illustrates the power of CT to reveal small cracks, even when they cannot be detected in any single radiograph. The match lines between the two halves of the polyethylene cylinder are visible in both data sets, even though they are nominally in contact. We've seen this in other cases, including ~10-MV neutron imaging of this polyethylene test object.

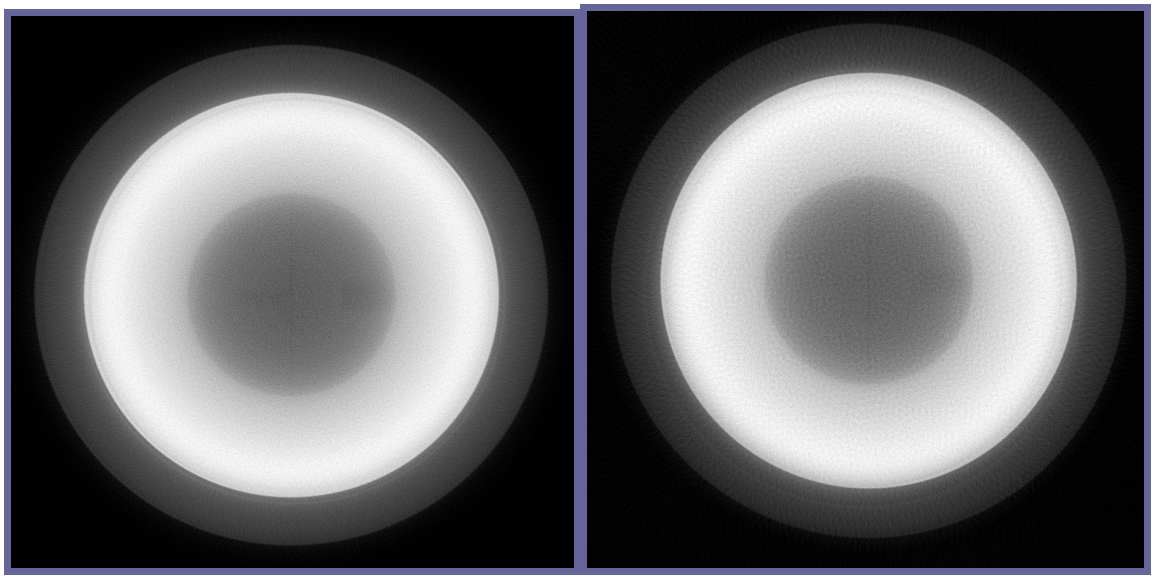

Figure 12 **Horizontal slices through 9-MV scan (left) and 15-MV scan (right) of Al-Pb-polyethylene test object.**

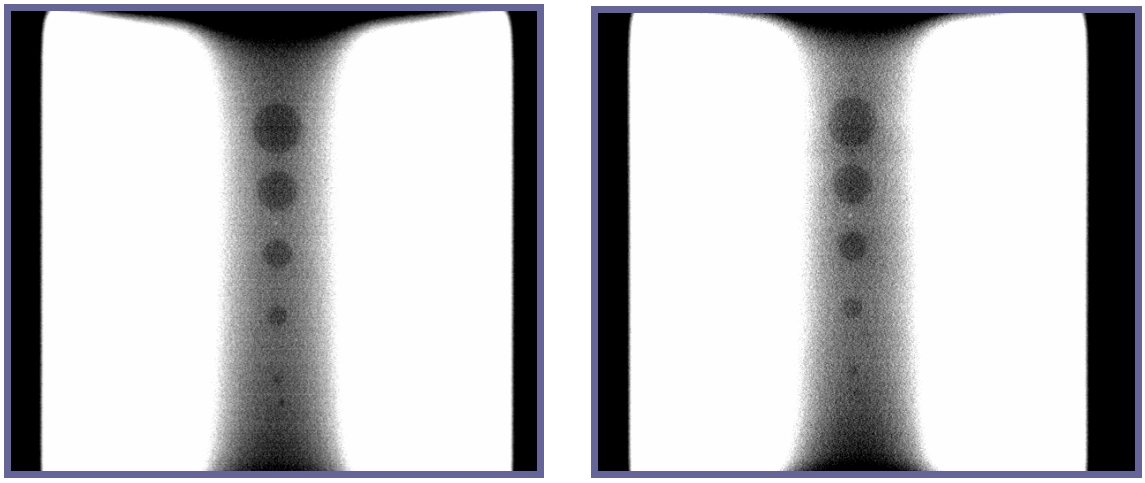

Figure 13 **Comparison of average of vertical CT slices for outside holes in the polyethylene for 9-MV scan (left) and 15-MV scan (right) of Al-Pb-polyethylene test object.**

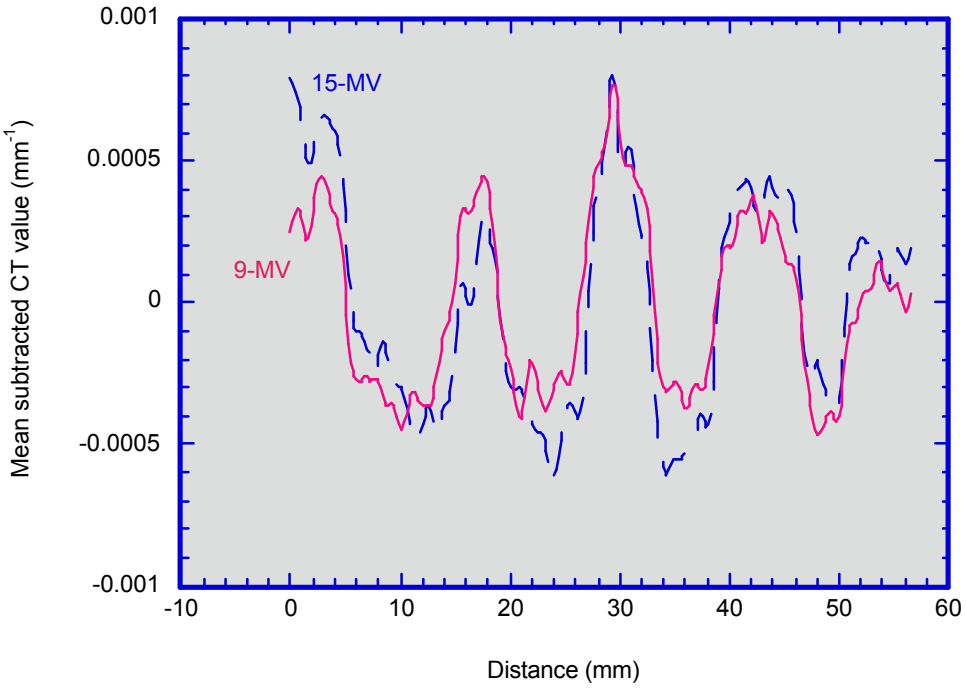

Figure 14 **Comparison of lineouts through outside holes in polyethylene from Figure 13.**

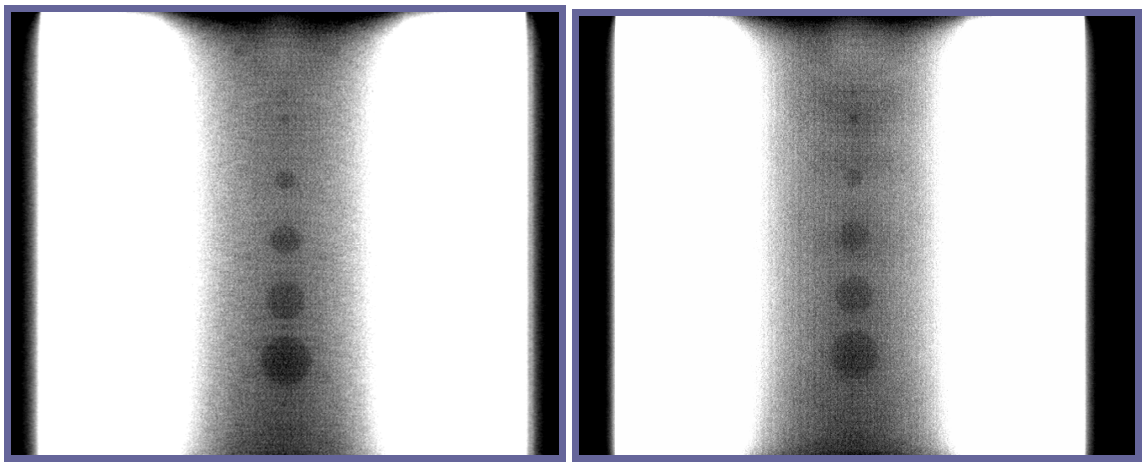

Figure 15 **Comparison of average of vertical CT slices for center holes in the polyethylene for 9-MV scan (left) and 15-MV scan (right) of Al-Pb-polyethylene test object.**

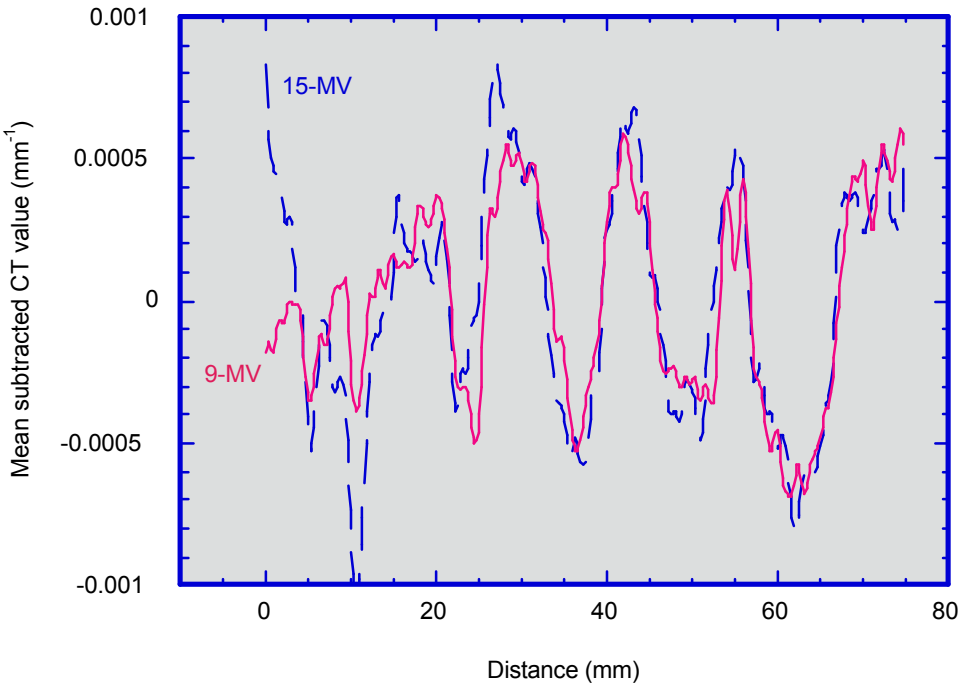

Figure 16 **Comparison of lineouts through outside holes in polyethylene from Figure 15.**

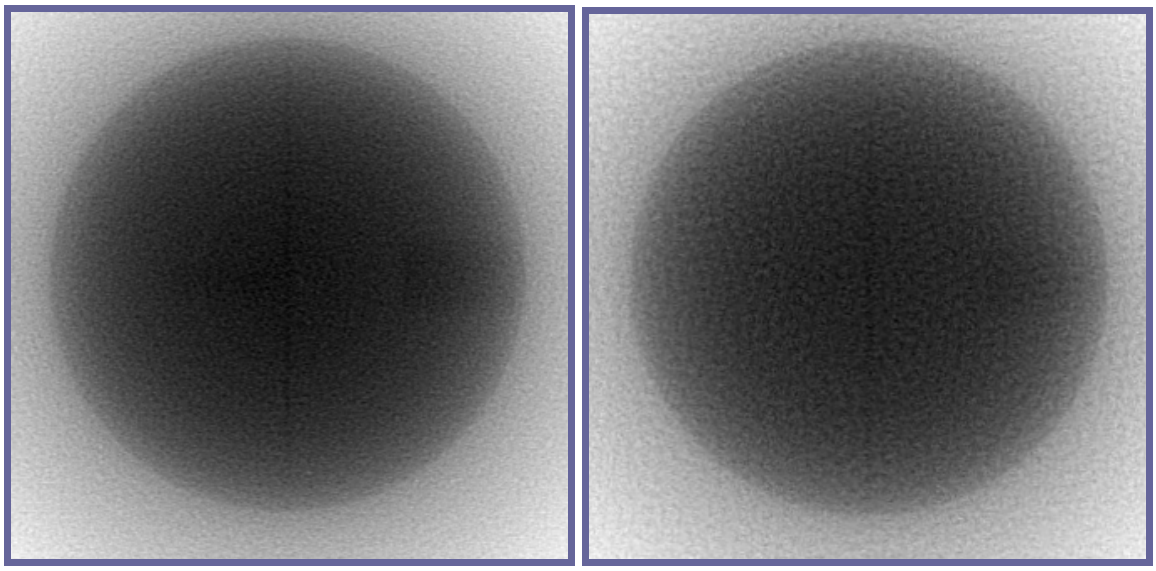

Figure 17 **Extracted center regions of horizontal slices of 9-MV (left)and 15-MV (right) for Al-Pb-polyethylene test object showing larger pattern noise in 15-MV data.**

Al-Pb-Poly+ W ring

For the second assembly we added the AWE tungsten ring as indicated in the drawing in Figure 3. Two aspects of this assembly are of interest here, the quality of the imaging for the features in the polyethylene shadowed by the tungsten ring, and the features on the inner wall of the tungsten ring itself. Figure 18 contains vertical slices through the center holes. Figure 18 contains vertical slices through the outside holes in the polyethylene.

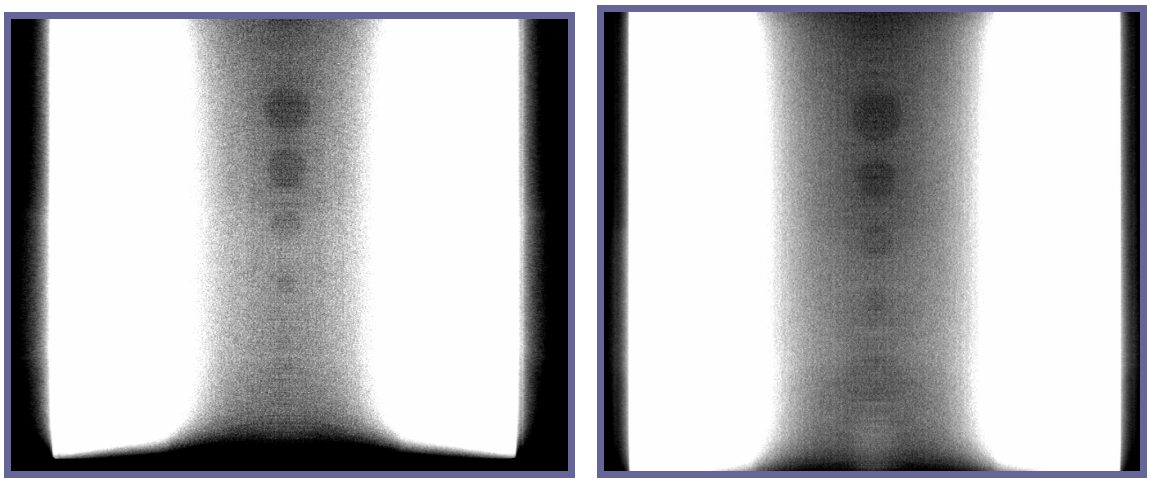

Figure 18 **Comparison of 9-MV (left) and 15-MV (right) vertical slices through the center holes in the polyethylene for the Al-Pb-polyethylene + W assembly.**

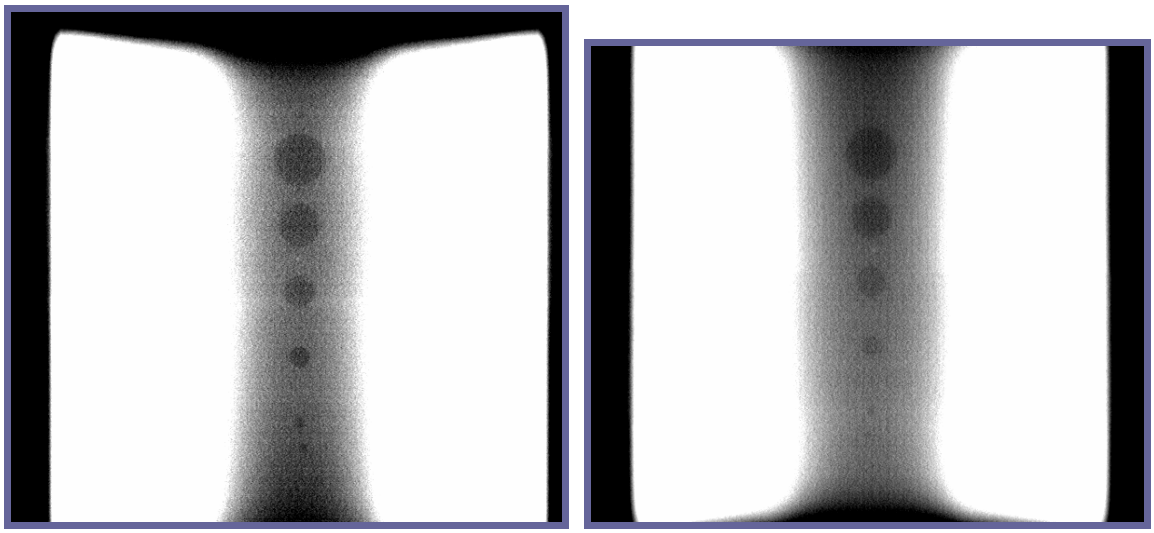

Figure 19 **Comparison of 9-MV (left) and 15-MV (right) vertical slices through the outside holes in the polyethylene for the Al-Pb-polyethylene + W assembly.**

The center holes in the 9-MV data set are barely distinguishable from the rest of the poly-material. The 15-MV data is only slightly better. This is consistent with the expectation that additional scatter and attenuation will degrade fidelity in the center of the

assembly. The signal-to-noise calculated from a rectangular area in the polyethylene in the shadow of the tungsten ring, are 26 for the 9-MV data, and 36 for the 15-MV data. Both data sets provide more detail on the outside holes of the polyethylene. The 650-μm drill bit is visible in each data set, and the 0.9-mm hole is just at the limit of what can be resolved for the contrastive difference between air and polyethylene. Signal to noise in the slices covering the outside holes is 56 for the 9-MV data and 49.52 for the 15-MV results. The additional attenuation provided by the tungsten ring generates enough scatter and attenuation to just about wash out features in the center of the assembly for the 9-MV spectra, with the signal-to-noise measuring lower than the 15-MV data. However, for the outside holes where there is enough signal to gain a measurement of features, the 9-MV data is less noisy, as was the data acquired for the Al-Pb-polyethylene assembly scanned without the tungsten ring.

Figures 20 and 21 present horizontal slices through the section of the tungsten ring with the holes for the two scans. Neither scan imaged the 250-μm holes. Other features in the tungsten ring are imaged in both the 9-MV and 15-MV data sets. As expected, the 15-MV data displays less spatial resolution and slightly more contrast. The diameter of the AWE ring emphasizes the impact of the larger spot size in the 15-MV linac. Figure 22 presents lineouts from a shell extraction within the tungsten ring.

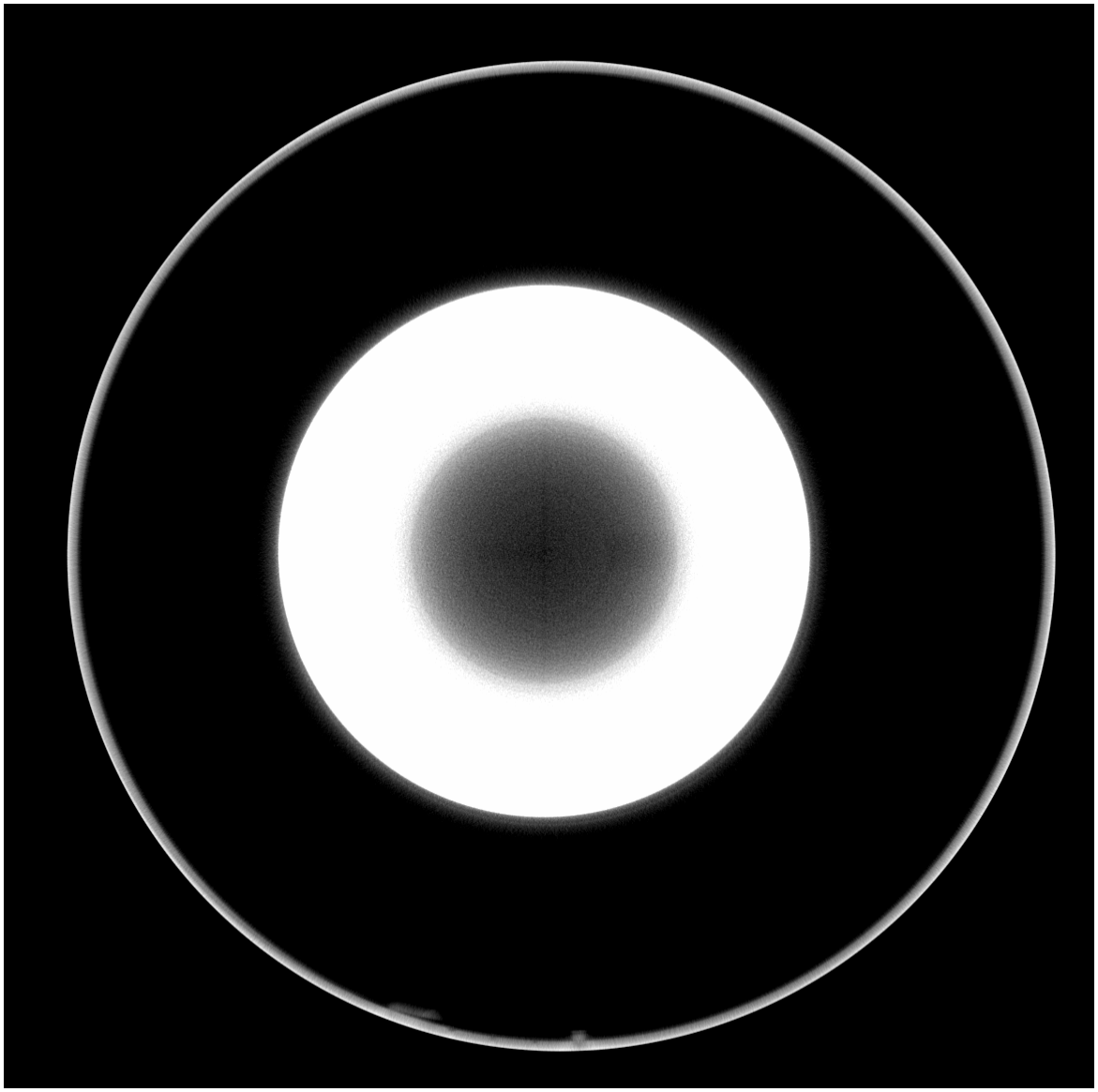

Figure 20 **Horizontal slice through Al-Pb-polyethylene + W ring showing identification of mm holes in the W ring. Data acquired at 9 MV.**

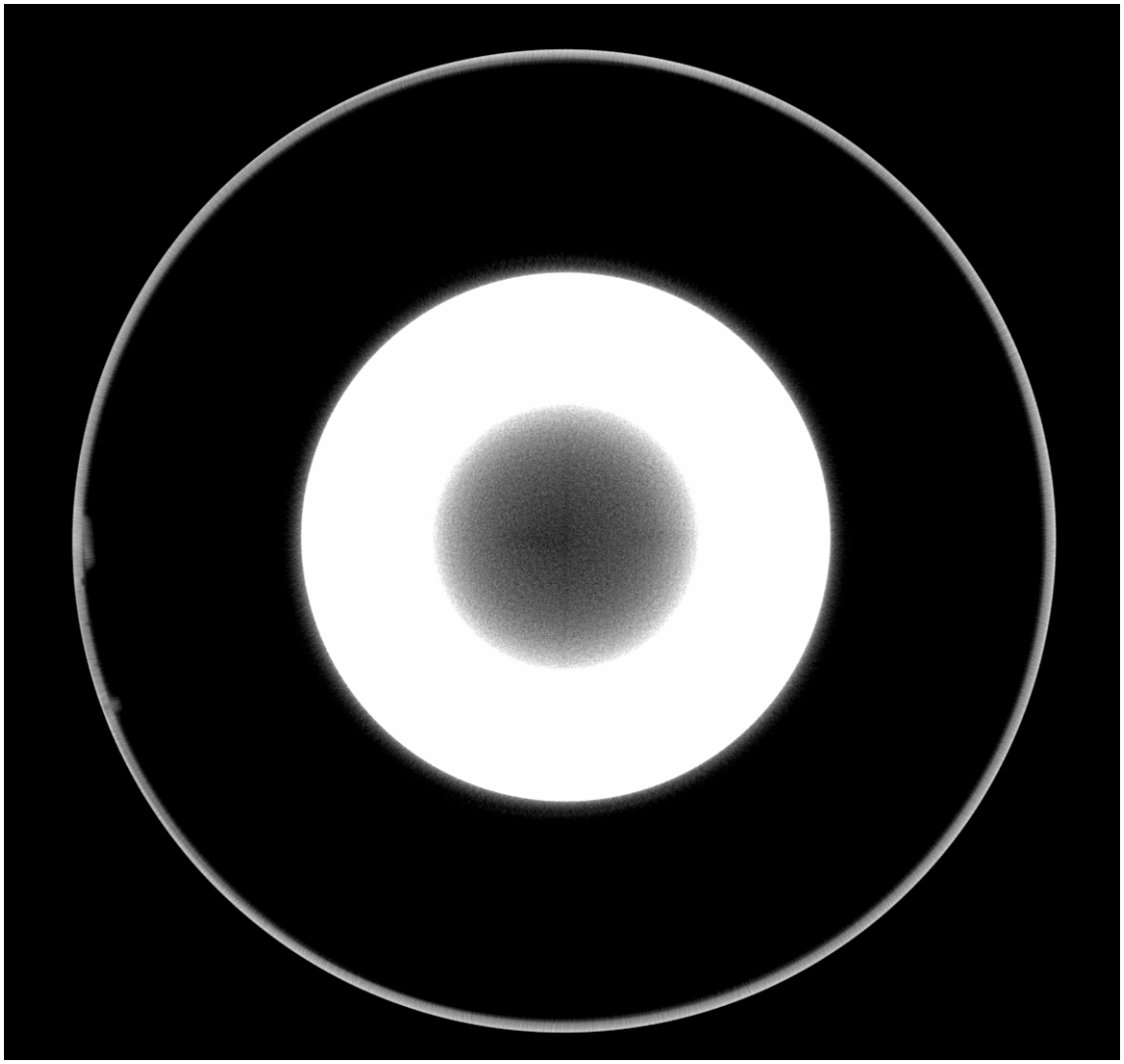

Figure 21 **Horizontal slice through Al-Pb-polyethylene + W ring showing identification of mm holes in the W ring. Data acquired at 15 MV.**

Figure 22 **Comparison of lineouts through holes in W ring.**

Al-Pb-polyethylene + W ring + 2 stainless steel rings

In this third assembly, the additional attenuation from the two 0.5-inch-thick stainless steel rings is sufficient to render the features in the polyethylene below the threshold of visibility for the 9-MV scan. The 15-MV data is only slightly better. Figure 23 presents vertical slices through the center holes of the polyethylene insert for both data sets. Figure 24 presents vertical slices through the outside holes in the polyethylene for data from the two energies. Figures 23 & 24 are heavily processed to remove cupping in order to enable some visualization of holes. The price of this processing is to introduce artifacts at the outer edges of the images. Even with these enhancements the large holes are barely visible. The signal-to-noise for the different energies is comparable, 31 for the 9-MV data and 34 for the 15-MV data. Figures 25 and 26 present horizontal slices through the entire assembly in the region with the features in the tungsten ring. The 1-mm features in the tungsten ring are identifiable in both data sets.

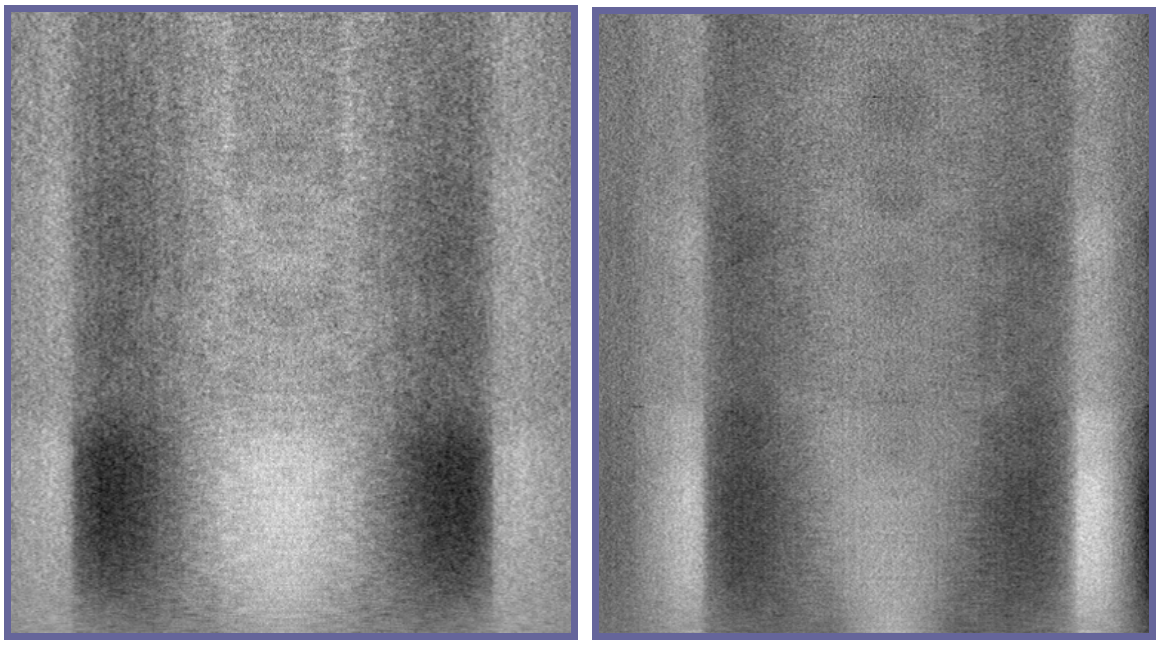

Figure 23 **Comparison of vertical CT slices containing center holes. Assembly is Al-Pb-polyethylene + W ring + 2 stainless steel cylinders. Nine-MV data on left and 15-MV data on the right.**

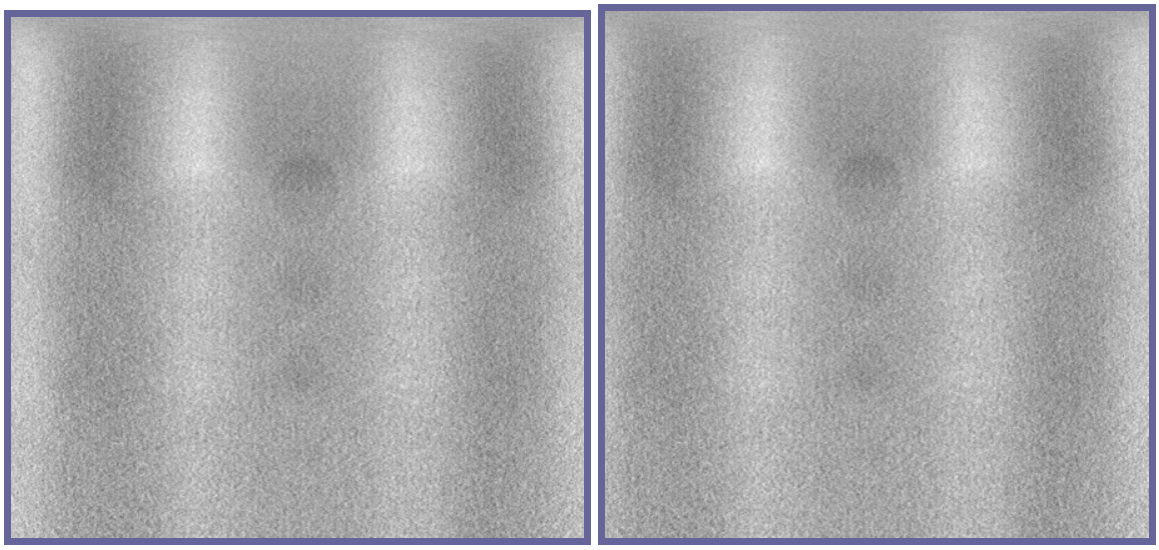

Figure 24 **Comparison of vertical CT slices containing outside holes. Assembly is Al-Pb-polyethylene + W ring + 2 stainless steel cylinders. Nine-MV data on left and 15-MV data on the right.**

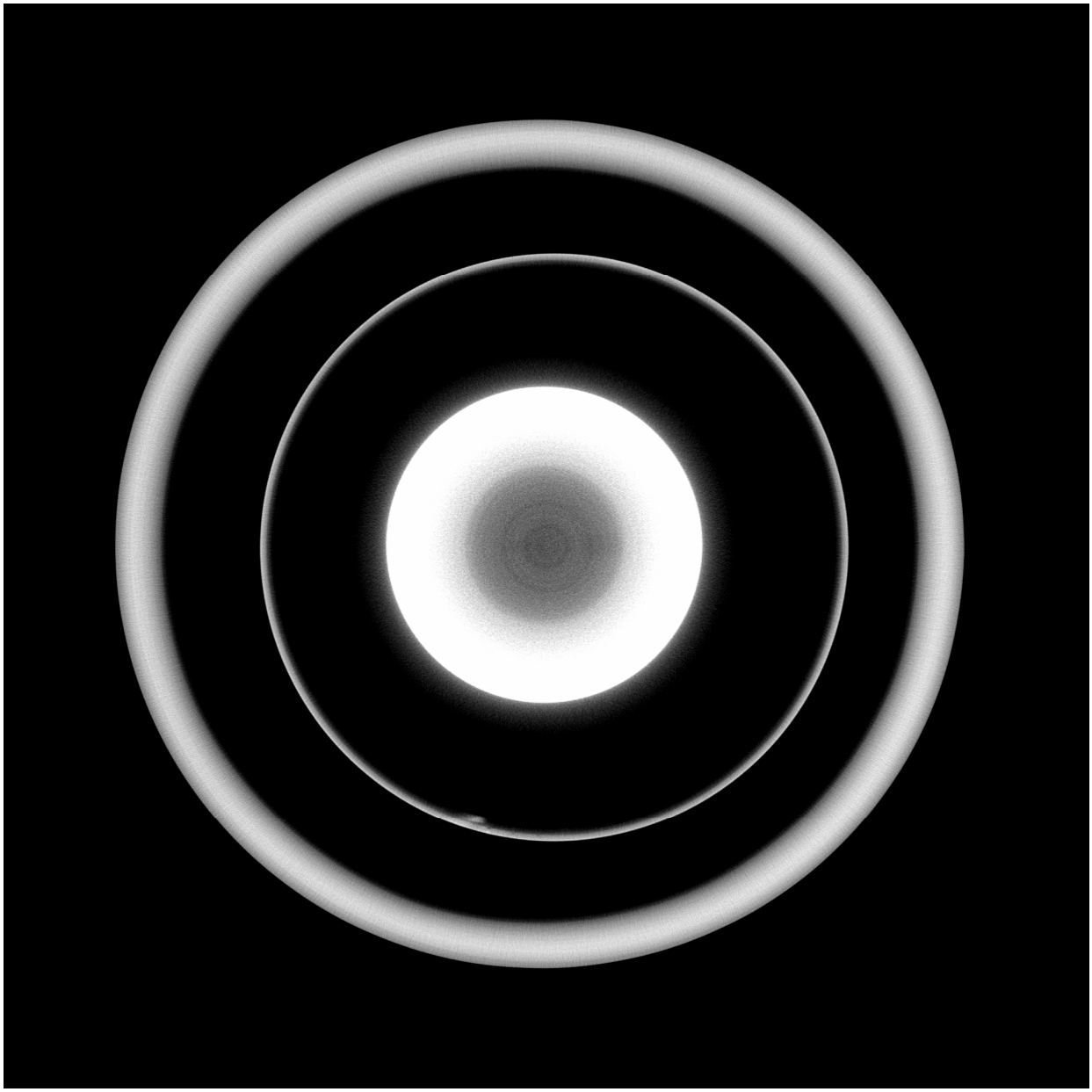

Figure 25 **Cross sectional slice through Al-Pb-polyethylene + W ring + 1 stainless steel cylinder showing identification of mm holes in the W ring. Data were acquired with 9-MV spectrum.**

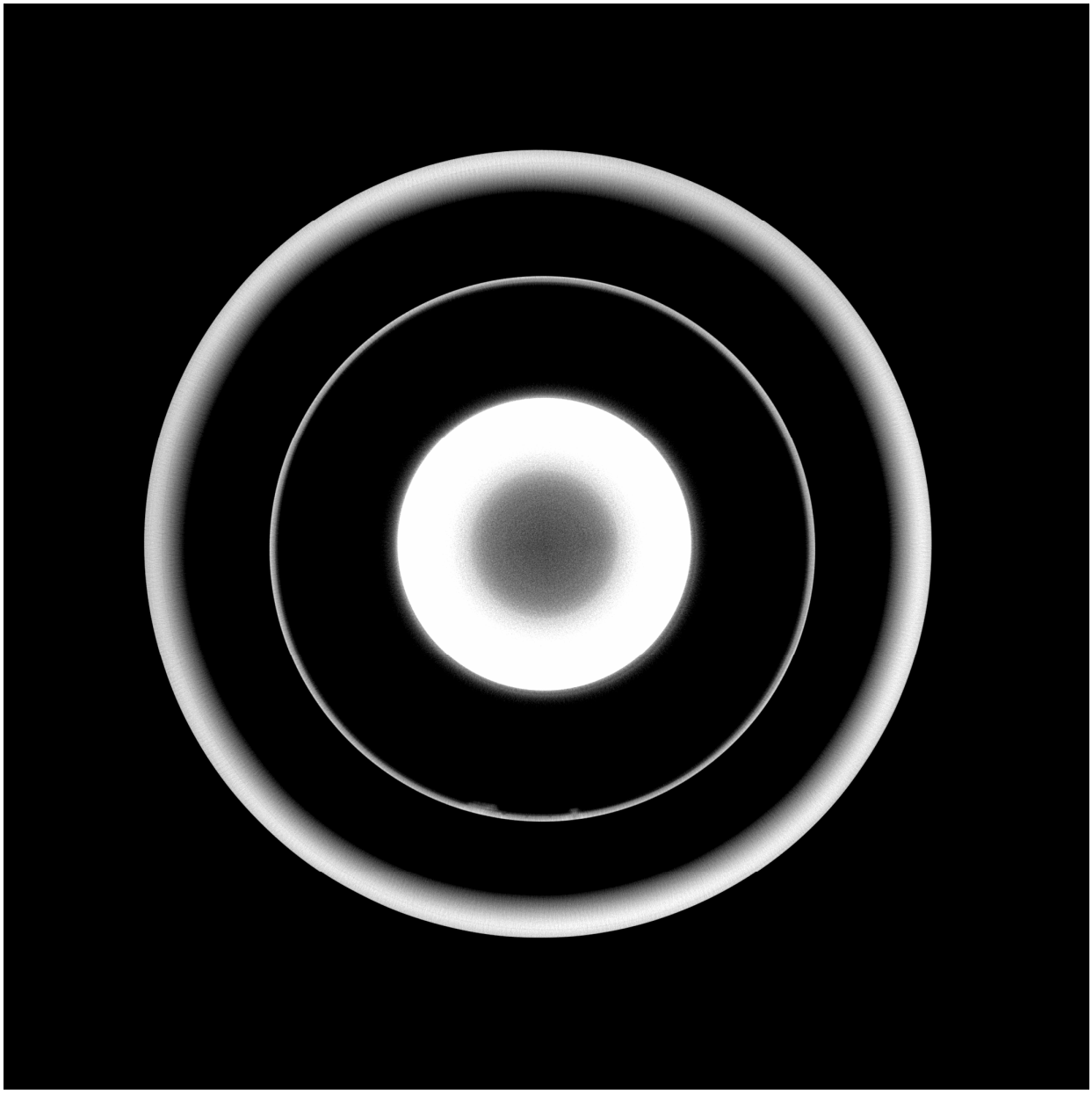

Figure 26 **Cross sectional slice through Al-Pb-polyethylene + W ring + 1 stainless steel cylinder showing identification of mm holes in the W ring. Data were acquired with 15-MV spectrum.**

Discussion

We expected higher room return effects at Hill AFB because of the size and design of the bay in which the linac is operated. At first glance radiographic data suggest that room scatter may be less at Hill than at LLNL because observed attenuation is greater (Figure 11). But, "it ain't that simple" *[Martz, 1986]*. One possibility is that albedo from the beam dump area is high at Hill AFB. This causes the bright field image to be artificially high. All radiographs are ratioed to the bright field image. With the object in place, much of the radiation that would otherwise reach the beam dump is attenuated in the object, reducing the beam dump return and making the radiograph appear to have excess attenuation. Of the many possible explanations for the greater radiographic attenuation using a 15-MV spectrum, we believe the most likely is an artifact of the design of the bay at Hill.

The pattern noise in the 15-MV data is puzzling and unexpected. It seems to not be random noise, though we make this observation with reservation since we've been fooled before. It also seems to not arise from positional shift of any geometry or else spatial resolution in the CT data would be compromised. We correct each radiograph for average intensity by using an unattenuated region. If the source has structure on a time scale between the read time of a single column and the time interval between frames, this procedure is not adequate when using the Thales panel. This effect is subtle and requires some effort to understand. Basically, the panel has a rolling read out. The Am-Si panel is always "on". There is no shutter. Each column is read in sequence. Each column has the same integration interval, but it is a time-displaced for each column of the image.[4] Once a read cycle is completed, the panel integrates for a period, then begins to read again. To make a simple example, assume the panel takes 1 s to read the entire image and that the integration time is set at 2 s. If the source is off for 100 ms during a read procedure, 90% of the columns have a uniform 5% loss in signal. The other 10% have a progressive loss ranging from 0% to 5%. The residual loss then overflows into the next image in the time sequence. Nothing of this magnitude occurred, but source temporal variations could have messed with the data if the Hill AFB linac is less stable than the LLNL linac.

Operational constraints caused interruption of the scans at Hill. The linac seemed to come back to the same position and performance but this is a difference between the work at LLNL and that at Hill. At Hill, we did not acquire additional bright field images at the time operation was resumed after an interruption. If the scintillator has significant time and dose dependent behavior, this would introduce a normalization oddity. It is not unusual for scintillators to get brighter with continued radiation dose and then to have afterglow at the cessation of radiation dosing. We've have observed this in Lanex screens, but we've never characterized or documented this behavior.

The field flattener used at Hill AFB is a large unknown in understanding this work. It imposed attenuation and spectral modification that depend on the angle to the beam axis. In addition, it is a major source of scatter. At the most important energy for image

[4] This effect will be familiar to those old timers familiar with taking film images of moving object using a camera equipped with a focal plane shutter.

formation, 3.5 MeV, 98% of the primary x-rays interact in the field flattener (on axis). How this affects CT data after reconstruction is a problem that one should not try to solve in one's head. This is a fruitful area to explore with Monte Carlo simulations and experiments. We found published Monte Carlo and experimental studies of the design and dose effects of field flatteners *[Quianteng, 2003; Mohan, 1985]* but these were concerned with therapy beams and did not consider the effects on imaging.

Results from the comparison scans were mixed, showing promise for 15-MV scanning, with some reservations. Sub-millimeter features were imaged in both spectra, with the 15-MV results retaining good fidelity with increasing chord lengths. Further, the 15-MV data presented better contrastive performance for the small features in the polyethylene. However, the noise content of the 15-MV data was higher than the 9-MV data, and the spatial resolution of the 15-MV data is less. We attribute the majority of this difference in spatial performance to source spot size and filtering (field flattener) differences. Secondly, the bay at Hill AFB is inferior to the LLNL bay.

The slightly poorer performance of the 15-MV scans notwithstanding, these data point to potentially better imaging performance for highly attenuating objects using a 15—MV source. It is our judgment that if sufficient attention were given to design of the bay, beam dump, collimation, filtration and linac spot size; a 15-MV imaging system using a flat panel could be developed with spatial resolution of 5 lp/mm and contrastive performance better that we have demonstrated using a 9-MV spectrum. The linac should have 0.4 mm spot size. This would permit using a source to object distance of 4.5 m and a source to detector distance of 6.0 m. The bay should be large and the beam 2 m above the heavy floor. High-Z material should be used wherever primary beam is incident. The linac should have secondary external shielding. Collimation must be exquisite. The beam dump should be a He-filled tube with a Pb plate >15 m from the detector.

Acknowledgements

We acknowledge consultations with Richard Watson, Hannah White, Duncan Maitland and Paul Tatum, all from AWE. We are grateful to AWE for the loan of the W ring. James E. Clayton, Varian Medical Systems, offered thoughts on the effect of the field flattener and provided details of material and shape.

This work was performed under the auspices of the U.S. Department of Energy by University of California, Lawrence Livermore National Laboratory under Contract W-7405-Eng-48.

References

[Aufderheide, 2000] M. B. Aufderheide III, J. Jackson, D. Goodman, D. Slone, H. Martz, A. Schach von Wittenau, C. Logan and J. Hall, *"HADES/CCG–A New Tomographic Reconstruction Tool,"* 27th Annual Review of Progress in Quantitative Nondestructive Evaluation, Ames IO, UCRL-JC-139604 (2000).

[Aufderheide, 2002] Maurice B. Aufderheide III, Harry E. Martz Jr., Dale M. Slone, Jessie A. Jackson, Alexis E. Schach von Wittenau, Dennis M. Goodman, Clinton M. Logan, and James M. Hall, "*Concluding Report: Quantitative Tomography Simulations and Reconstruction Algorithms",* UCRL-146938, (2002).

[Grodzins, 1983] L. Grodzins, *"Optimum Energies for X-ray Transmission Tomography of Small Samples,"* Nuc. Instr. Meth. **206**: 541-545, 1983.

[Logan, 2001] C. M. Logan and A. E. Schach von Wittenau, *"Effects of Backshield Albedo on Imagery with a dpiX Flashscan20 Using a 9-MV Bremsstrahlung Spectrum,"* Materials Evaluation **59:5**, 617-20 (2001).

[Martz, 1986] Personal communication, Harry E. Martz, Jr. (1986).

[Martz, 2002] Harry E. Martz, Jr., Clinton M. Logan and Peter J. Shull, *"Radiology,"* in Nondestructive Evaluation: Theory, Techniques and Applications, Peter J. Shull, Editor. Marcel Dekker, Inc., New York, NY, (2002).

[Mohan, 1985] Radhe Mohan, Chen Chui and Leon Lidofsky, *"Energy and angular distributions of photons from medical linear accelerators"*, Med. Phys. **12:5** (1985).

[Monnin, 2005] P. Monnin, D. Gutierrez, and S. Bulling, *"Performance comparison of an active matrix flat panel imager, computed radiography system, and a screen-film system at four standard radiation qualities"*, Med. Phys. **32:2**, 2005.

[Quanfeng, 2003] Li Quanfeng and Yan Huiyong, *"Monte Carlo design of X-ray flattening filters"*, Journal Tsinghua University, **43:6**, p 732-734 (2003). Chinese.

[Schach von Wittenau, 2001] A. E. Schach von Wittenau and C. M. Logan, *"Nine Megavolt Linac Radiography in Pantex Bay 19: Scatter from Collimators and Environment",* UCRL-ID-146128, (2001)

[Schach von Wittenau, 2002a] A. E. Schach von Wittenau, C. M. Logan and R. D. Rikard, *"Using a W Rollbar to Measure the Source Spot Size of a 9 MV Bremsstrahlung Linac"*, Med. Phys. **29:8,** p.1797 (2002).

[Schach von Wittenau, 2002b] A.E. Schach von Wittenau, C. M. Logan, M. B. Aufderheide and D. M. Slone, *"Blurring Artifacts in Megavoltage Radiography with a Flat-Panel Imaging System: Comparison of Monte Carlo Simulations with Measurements"*, Med. Phys. **29:11** (2002).

[Schach von Wittenau, 2002c] A.E. Schach von Wittenau, *"Edge-spread functions expected for several changes in a commercial flat-panel system",* UCRL-ID-147751, 2002.

[Schach von Wittenau, 2005] Personal Communication: *"Spectrum for 15 MV computed using MCNP4C for 15-MeV electrons incident on 1.4 mm of tungsten"*.

[Siewerdsen, 2001] J.H. Siewerdsen and D. A. Jaffray, *"Cone beam computed tomography with a flat panel imager: Magnitude and effects of x-ray scatter"*, Med. Phys. **28:2** (2001).

[Waters, 1999a] A. Waters, B. Graybeal, H. Saleh, H. Martz, C. Logan, D. Rikard and R. Green, *"Qualitative Comparison of NDE Techniques for the Inspection of Bridge Pins,"* Proceedings of the 9th Annual Symposium on Nondestructive Characterization of Materials, Sydney, Australia (1999).

[Waters, 1999b] A. Waters, H. Martz, C. Logan, E. Updike and R. Green, *"High Energy X-Ray Radiography and Computed Tomography of Bridge Pins,"* Proceedings of 2nd Japan-U.S. Symposium on Advances in Nondestructive Testing, Oahu, HI, UCRL-JC-132822 (1999).

•••

•••